nanomaterials

MDPI

Article

Cu@Pd/C with Controllable Pd Dispersion as a Highly Efficient Catalyst for Hydrogen Evolution from Ammonia Borane

Yanliang Yang [1,*], Ying Duan [2], Dongsheng Deng [1], Dongmi Li [1], Dong Sui [1] and Xiaohan Gao [3,*]

1 Henan Key Laboratory of Function-Oriented Porous Materials, College of Chemistry and Chemical Engineering, Luoyang Normal University, Luoyang 471934, China; dengdongsheng168@sina.com (D.D.); lidongmi223@126.com (D.L.); suidonghy@mail.nankai.edu.cn (D.S.)
2 College of Food and Drug, Luoyang Normal University, Luoyang 471934, China; duanying@mail.ustc.edu.cn
3 School of Chemistry and Material Science, College of Chemistry, Chemical Engineering and Environmental Engineering, Liaoning Shihua University, Fushun 113001, China
* Correspondence: yangyli@mail.ustc.edu.cn (Y.Y.); gaoxhan@163.com (X.G.)

Received: 19 August 2020; Accepted: 14 September 2020; Published: 16 September 2020

Abstract: A series of Cu@Pd/C with different Pd contents was prepared using the galvanic reduction method to disperse Pd on the surface of Cu nanoparticles on Cu/C. The dispersion of Pd was regulated by the Cu(I) on the surface, which was introduced by pulse oxidation. The Cu_2O did not react during the galvanic reduction process and restricted the Pd atoms to a specific area. The pulse oxidation method was demonstrated to be an effective process to control the oxidization degree of Cu on Cu/C and then to govern the dispersion of Pd. The catalysts were characterized by transmission electron microscopy (TEM), high-resolution transmission electron microscope (HRTEM), high angular annular dark field scanning TEM (HAADF-STEM), energy-dispersive spectroscopy (EDS) mapping, X-ray diffraction (XRD), X-ray photoelectron spectroscopy (XPS), auger electron spectroscopy (AES), and inductively coupled plasma optical emission spectrometer (ICP-OES), which were used to catalyze the hydrogen evolution from ammonia borane. The Cu@Pd/C had much higher activity than the PdCu/C, which was prepared by the impregnation method. The TOF increased as the Cu_2O in Cu/C used for the preparation of Cu@Pd/C increased, and the maximum TOF was 465 mol_{H2} min^{-1} $mol_{Pd}{}^{-1}$ at 298 K on $Cu@Pd_{0.5}$/C-640 (0.5 wt % of Pd, 640 mL of air was pulsed during the preparation of Cu/C-640). The activity could be maintained in five continuous processes, showing the strong stability of the catalysts.

Keywords: Pd dispersion; galvanic reduction; partial oxidation; ammonia borane

1. Introduction

Safe and convenient hydrogen storage is one of the key problems that have emerged in the application of hydrogen as clean energy. A lot of effort has been devoted to developing hydrogen storage materials, including physical and chemical storage systems, with excellent performance. Ammonia borane (AB), a stable solid in normal conditions with a hydrogen content of 19.6 wt %, was thought to be a potential chemical hydrogen storage material and has gained the attention of many scientists [1–10]. The AB could release 3 mol H_2 per mole AB at mild conditions in the presence of an appropriate catalyst.

A lot of catalysts were reported to be effective for the hydrogen evolution reaction from AB. Noble metals usually had very high activity for the hydrolysis of AB [11–40]. However, as noble metals are expensive, the full utilization of the noble metal atoms is a significant issue in the production

of noble metal-based catalysts. The non-noble metal-based catalysts were also used to catalyze the hydrolysis of AB, and the well-designed catalytic system had attractive activity for this reaction [41–55]. However, most of the non-noble metal-based catalysts had lower catalytic activity and less stability compared to the noble metals. Thus, attaining stable catalysts with highly activity and low cost was the aspirational aim for the hydrolysis of AB.

To reduce the consumption of noble metals, the addition of another non-noble metal was a useful option. The electronic structures of the noble metal catalysts could be modulated by the non-noble metal to obtain a more efficient bimetallic catalyst [30,56–64]. During the preparation of the bimetallic catalyst, burying the noble metal atoms in the metal nanoparticles should be avoided to get full utilization of the noble metals. The galvanic reduction method was an efficient approach to avert the embedment of noble metals, as the reduction reaction only occurred on the surface of non-noble metal. For example, Chen et al. achieved an atomically dispersion of Pt on the surface of Ni particles through the galvanic reduction method [62]. Dong et al. coated Co nanoparticles by Pt through the spontaneous displacement reaction of Co by Pt. As a result, the Pt covered the surface of Co nanoparticles only [57]. Both of the catalysts showed excellent catalytic activity on the hydrolytic dehydrogenation of ammonia borane.

The galvanic reduction method was an effective process to get a surface noble metal-rich catalyst [65–72]. However, when the pure metallic non-noble metal nanoparticles were used for the galvanic reduction process, the noble metal atoms tended to aggregate into large particles on the surface of the non-noble metal as on other supports. As a result, how to control the distribution of noble metals on the surface of non-noble metals needs further consideration. In this manuscript, based on our previous work on the preparation of Pd catalysts [73–78], we synthesized Cu@Pd/C with controllable Pd dispersion through the galvanic reduction method. The dispersion of Pd atoms on the surface of Cu nanoparticles was regulated by partial oxidation of the surface of Cu nanoparticles. The catalysts showed an initial turnover frequency (TOF) of 465 mol_{H2} min^{-1} $mol_{Pd}{}^{-1}$ at 298 K for the hydrolysis of AB, which was among the highest values in the literatures.

The preparation of Cu@Pd/C catalysts is illustrated in Figure 1. Firstly, Cu/C was synthesized by carbothermal reduction in N_2. Then, the surface of the Cu was partially oxidized to Cu(I) by the pulse injection of a limited amount of air at 473 K. The Pd was introduced to the surface of Cu particles by the displacement reaction of Cu(0) by Pd(II). As the displacement reaction was only conducted on Cu(0), the Pd(0) was confined to a limited area surrounded by Cu(I). As a result, the aggregation of Pd atoms to form larger particles was prevented by the surrounding Cu(I) species.

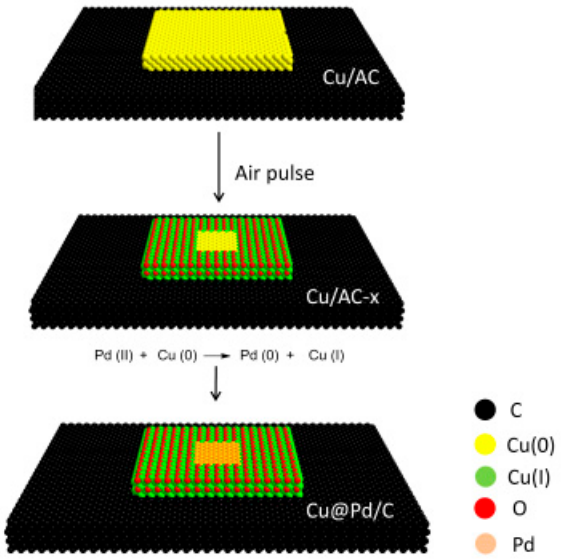

Figure 1. Procedure for the preparation of Cu@Pd/C.

2. Materials and Methods

2.1. Preparation of Catalysts

2.1.1. Cu/C

The Cu/C was prepared using the impregnation method. Typically, $Cu(NO_3)_2{\cdot}3H_2O$ (1.20 g) was dissolved in water (5.65 g) to form a homogeneous transparent solution. Then, AC (5.00 g, 100 mesh) was added into the solution and stirred into paste. After being dried at 373 K overnight, the solid was transferred into a tubular furnace and calcined at 773 K for 2 h in N_2 atmosphere to afford the Cu/C.

2.1.2. Cu/C-x

The Cu/C (1.00 g) was heated to 473 K in a tubular furnace under N_2 atmosphere. Then, the air was pulse-injected into the furnace at a rate of 40 mL min^{-1}. Eighty mL of air was introduced for each pulse, and the interval for each pulse was 1 min. After all the air needed was introduced, the sample was cooled to room temperature quickly in N_2. The sample was denoted as Cu/C-x, where x referred to the amount of air pulsed.

2.1.3. Cu@Pd_y/C-x

The $PdCl_2$ dissolved in dilute HCl (Pd, 0.5 wt %) was added dropwise into a suspension of Cu/C-x (0.50 g) in water (40 g) under N_2 atmosphere at room temperature. The suspension was stirred for 4 h and washed with water three times and then with ethanol once. The solid was dried under vacuum at 323 K to afford the Cu@Pd_y/C-x where y was the mass percent of Pd.

2.1.4. Pd_yCu/C

The Pd_yCu/C was prepared using the impregnation method: the same method used for Cu/C, except instead of the solution of $Cu(NO_3)_2{\cdot}3H_2O$ a solution of $PdCl_2$ and $Cu(NO_3)_2{\cdot}3H_2O$ was used. The following process was the same as the preparation of Cu/C.

2.2. Characterization

The high-resolution transmission electron microscope (HRTEM) and transmission electron microscopy (TEM) mappings were collected on a Tecnai G2 F20 (Hillsboro, OR, USA). The energy-dispersive spectroscopy (EDS) mappings were characterized by a JEM2100F (Tokyo, Japan) equipped with an EDS detector. The high angular annular dark field scanning TEM (HAADF-STEM) images were taken on a FEI Themis Z microscope (Hillsboro, OR, USA). The X-ray diffraction (XRD) patterns were obtained on a Rigaku D/Max 2500/PC powder diffractometer (Tokyo, Japan) with Cu Kα radiation (λ = 0.15418 nm) at 40 kV. The scanning rate was 5° min^{-1}. Inductively coupled plasma optical emission spectrometer (ICP-OES) was conducted on Agilent 5110 ICP-OES equipment (Santa Clara, CA, USA). The samples were calcined in air at 673 K before dissolution. X-ray photoelectron spectroscopy (XPS) and auger electron spectroscopy (AES) measurements were conducted on a Thermo Escalab 250Xi spectrometer (Waltham, MA, USA).

2.3. Catalytic Hydrolysis of AB

The catalytic hydrolysis of AB was conducted on a homemade reaction apparatus for monitoring hydrogen generation. Firstly, H_2O (9.5 mL) and catalyst (Pd, 0.45 mg) was loaded into the jacket reactor connected to constant temperature water. The reactor was charged and purged with N_2 for 3 times and stirred for 30 min at the desired temperature to reach thermal equilibrium. Then, the reaction was started by the introduction of a solution of AB (0.5 mL, 1 mmol) into the reactor. The volume of H_2 was monitored by introducing the gas to a calibrated glass tube at scale. The tube was surrounded by constant water (298 K), and the bottom of the tube was connected to a burette opening to the

atmosphere. The liquid level of the tube and the burette was controlled to the same height to ensure the pressure in the tube was maintained at 1 atmospheric pressure.

3. Results and Discussion

3.1. Charcaterization

The EDS mapping of Cu/C-320 is shown in Figure 2a–e. The Cu, C, and O were detected in the sample. The distribution of O did not always follow the distribution of Cu. In other words, the signal of O and Cu did not always appear in the same areas. This phenomenon can be explained in this way. When an area had the signal of Cu without O, it should be the signal for Cu(0). The simultaneous appearance of Cu and O was mostly as the oxidized Cu. So, both Cu(0) and oxidized Cu were contained in Cu/C-320 revealed by the EDS mapping. This result was confirmed by the XRD and HRTEM characterization. The diffraction peaks corresponding to both Cu and Cu_2O appeared in the XRD pattern of Cu/C-320 (Figure 3a). The HRTEM image of Cu/C-320 was exhibited in Figure 2f. The crystalline domains corresponding to both Cu (d_{111} = 0.210 nm) and Cu_2O (d_{110} = 0.305 nm) could be observed in the image. Based on the above characterization, the Cu/C-320 should possess a surface composed of Cu and Cu_2O after the pulse injection of air.

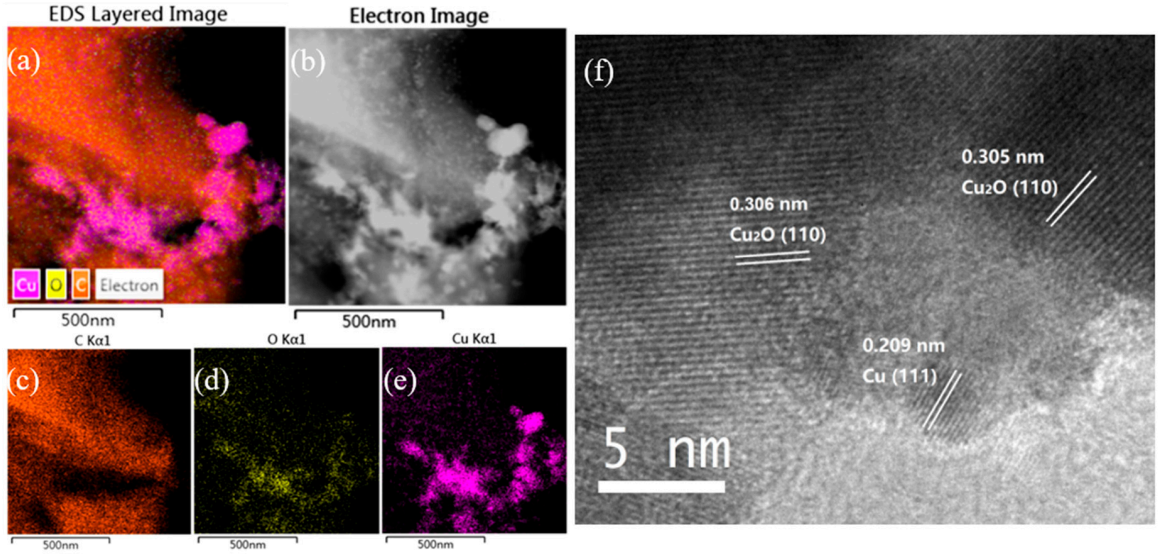

Figure 2. Energy-dispersive spectroscopy (EDS) mapping images (**a**–**e**) of Cu/C-320 and HRTEM (**f**) image of Cu/C-320.

The Cu@Pd/C-320 was prepared by the displacement of surface Cu(0) by Pd(II) in N_2. The theoretical contents of Pd were varied from 0.5 wt % to 2.0 wt %. The XRD patterns of Cu@Pd/C-320 are shown in Figure 3a. The diffraction peaks centered at 36.4°, 42.3°, 61.3°, and 73.5° were attributed to the diffraction of Cu_2O, while the peaks at 43.3°, 50.4°, and 74.1° were the diffractive peaks of metallic Cu. The diffraction peaks corresponding to Cu(0) decreased as the Pd content increased, implying the replacement of Cu(0) by Pd(II). The diffraction peaks of Cu_2O had broadened slightly while maintaining intensity as the Pd content increased, showing that the Cu_2O was steady during the replacement process. No peaks corresponding to Pd were detected, which should be caused by the high dispersion of Pd. The HRTEM also showed no crystalline domains of Pd for the Cu@$Pd_{0.5}$/C-320 and Cu@$Pd_{2.0}$/C-320 samples (Figure 3b). As the Cu(0) was surrounded by Cu(I), only very little Pd(II) could be reduced at a special area. After the displacement, the Pd(0) had little chance to get together, as they were cut apart by the Cu(I). The EDS mappings of Cu@Pd/C-320 are displayed in Figure 3c–g and Figure S1–S3. The Pd had uniform distribution in all four samples with different Pd content. After careful analysis of the element distribution in the EDS mappings, it could be seen that

the Pd mostly embedded on the surface of Cu nanoparticles. In the area determined in the blue box in $Cu@Pd_{0.5}/C$-320 (Figure 3c), the Pd was surrounded by O, which should have originated from the Cu_2O. This was clear proof for the assumption that the Cu_2O divided the surface of Cu(0) and surrounded the Pd to prevent the aggregation of Pd atoms. The distribution of Pd on Cu was characterized by HAADF-STEM, and the result is shown in Figure 3h–i. Both single Pd atoms and two-dimensional clusters can be seen in the HAADF-STEM images. This showed that the strategy was effective for the preparation of Pd catalysts with high Pd dispersion.

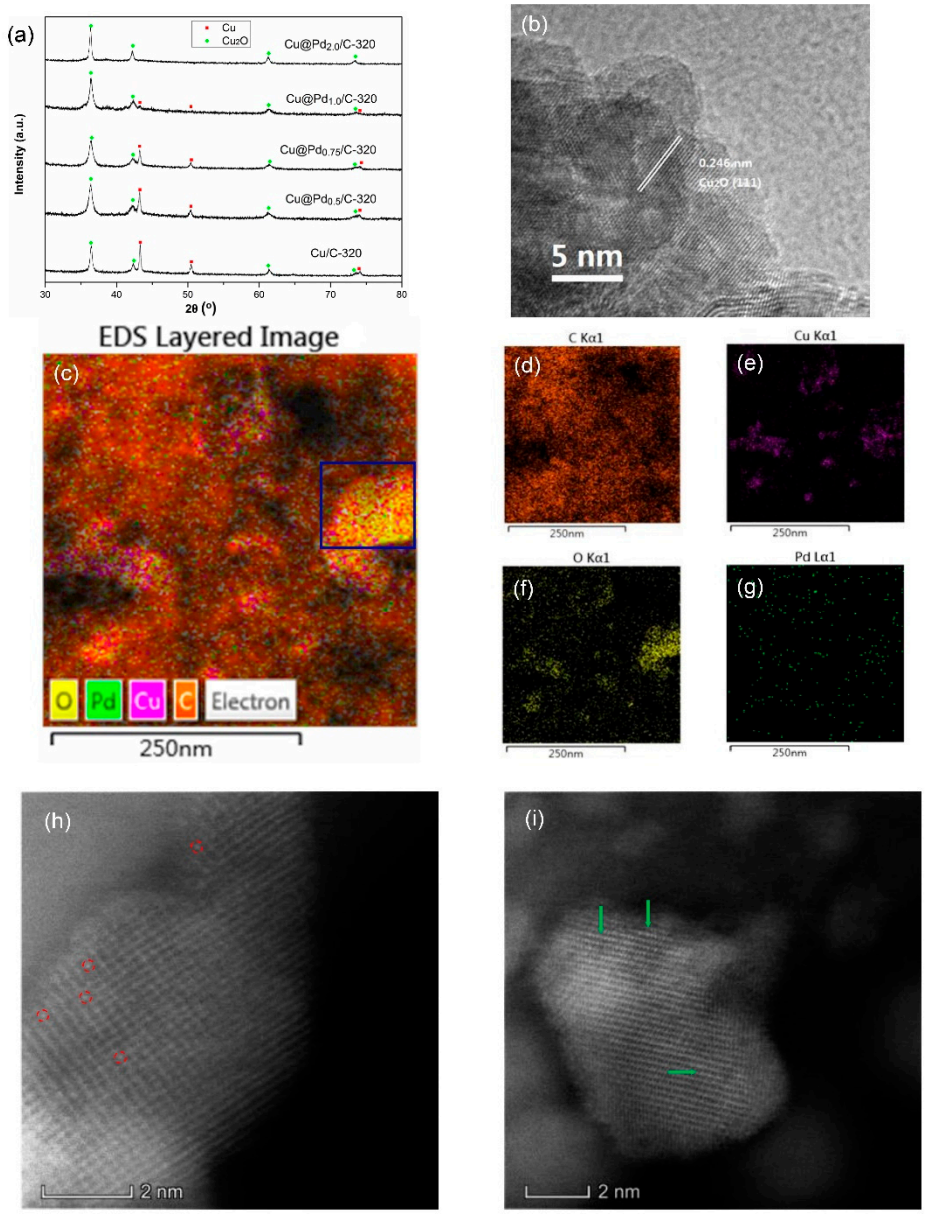

Figure 3. XRD patterns (**a**) of Cu@Pd/C-320, HRTEM (**b**), EDS mapping images (**c**–**g**), and high angular annular dark field scanning TEM (HAADF-STEM) images (**h**,**i**) of $Cu@Pd_{0.5}/C$-320. The single Pd atoms (indicated by red circles) and Pd clusters (indicated by green arrows) could be seen in the HAADF-STEM images.

To make a comparison, the PdCu/C catalysts were prepared through the impregnation method with the same theoretical contents of Pd as Cu@Pd/C-320. The XPS spectra of Cu@Pd/C-320 and PdCu/C-320 are displayed in Figure 4. The binding energy at 336.4 eV and 341.9 eV were assigned to pd $3d_{5/2}$ and pd $3d_{3/2}$ [79,80]. The Cu/C-320 had no signal of Pd. The intensity of the Pd signal

increased as the Pd content increased for both Cu@Pd/C-320 and PdCu/C. However, the Cu@Pd/C-320 had higher intensity peaks at 336.4 eV and 341.9 eV than that of PdCu/C at the same content of Pd. As only the surface photoelectrons could escape from the sample, the XPS characterization showed the surface composition of samples. The higher peaks intensity showed that the Cu@Pd/C-320 possessed a Pd-rich surface comparing to PdCu/C.

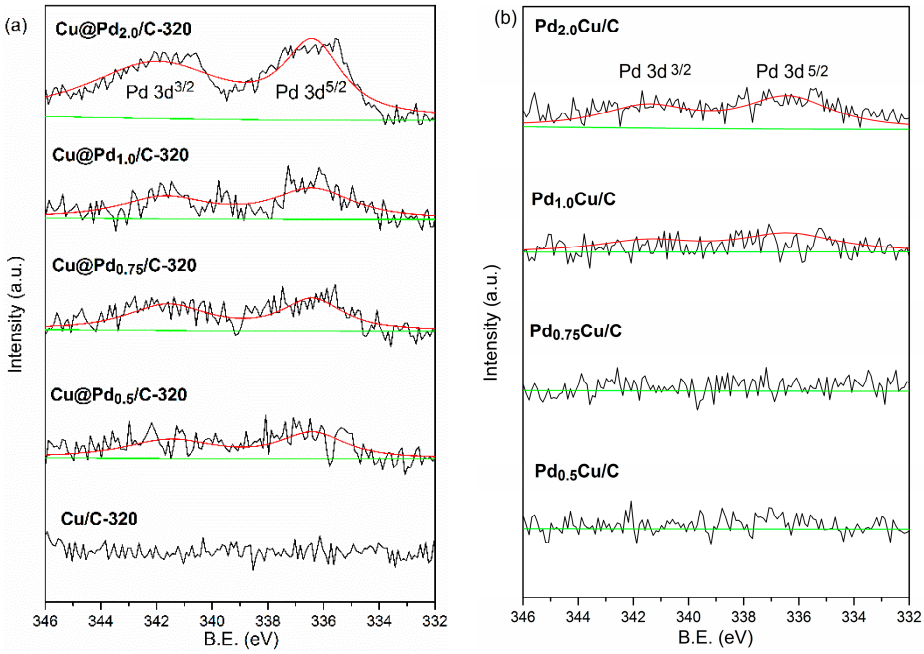

Figure 4. XPS spectra of Cu@Pd/C-320: Cu/C-320 (**a**), and PdCu/C (**b**).

3.2. Hydrogen Evolution from AB

The hydrogen evolution reaction was conducted on a homemade device, as shown in Figure S15. Both the Cu@Pd/C and PdCu/C were employed as the catalysts for the hydrolysis of AB at 298 K, and the results are shown in Figure 5a. The activated carbon had no activity for the hydrolysis of AB, and the commercial Pd/C had a low hydrogen evolution rate (3.5 mol_{H2} min^{-1} $mol_{Pd}{}^{-1}$) in the reaction conditions. The $Cu@Pd_{0.5}$/C-320 achieved a TOF of 306 mol_{H2} min^{-1} $mol_{Pd}{}^{-1}$ at 298 K, which was twice as much as that of $Pd_{0.5}Cu$/C (149 mol_{H2} min^{-1} $mol_{Pd}{}^{-1}$) at the same conditions. As the content of Pd increased to 2.0%, the TOF of $Pd_{2.0}Cu$/C decreased sharply to 53 mol_{H2} min^{-1} $mol_{Pd}{}^{-1}$, while that of $Cu@Pd_{2.0}$/C-320 decreased very slowly to 256 mol_{H2} min^{-1} $mol_{Pd}{}^{-1}$. The difference in the activity between PdCu/C and Cu@Pd/C-320 should be caused by the different Pd distribution. As the hydrolysis of AB happened on the surface of the catalysts, the activity mostly depended on the surface Pd content. The Pd was mainly distributed on the surface of Cu nanoparticles in Cu@Pd/C-320, while some of the Pd atoms may be buried in the Cu nanoparticles for PdCu/C. As a result, the Cu@Pd/C-320 had higher TOF than that of PdCu/C. As the content of Pd increased, more Pd atoms would be buried in the nanoparticles for PdCu/C, leading to the sharp decrease in TOF. On the other hand, the galvanic reduction method ensured that most of the Pd atoms distributed on the surface for Cu@Pd/C-320, disregarding the content of Pd. As a result, the activity decreased a little as the Pd content increased. Similar trends were obtained as the reaction temperature increased from 298 to 313 K. The hydrolysis of AB catalyzed by Cu@Pd/C-320 and PdCu/C were conducted at 298, 303, 318, and 313 K respectively (Figure 5a and Figures S5–S8). The TOF on Cu@Pd/C-320 was much higher than the TOF on PdCu/C with the same Pd content at different temperatures (Figure 5b,c). The TOF on Cu@Pd/C-320 remained steady, while that on PdCu/C decreased sharply as the contents of Pd at a certain temperature increased. The activation energy (*Ea*) was calculated based on the Arenius formula (Figure 5b,c). It was found that both the Cu@Pd/C-320 and PdCu/C had similar *Ea* values (around 60 kJ mol^{-1}). This implied that

the catalysts might have similar active site considering the similar composition of the catalysts, and the difference in TOF should not be caused by the change in *Ea*.

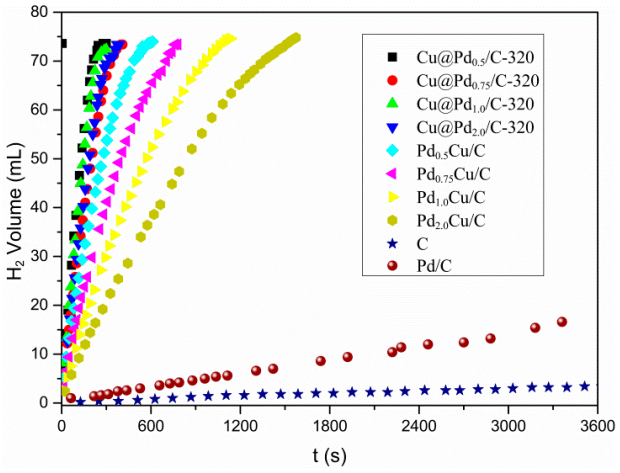

(**a**)

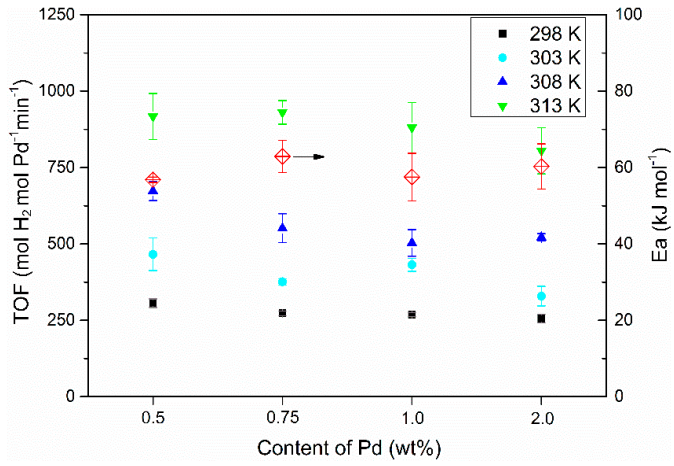

(**b**)

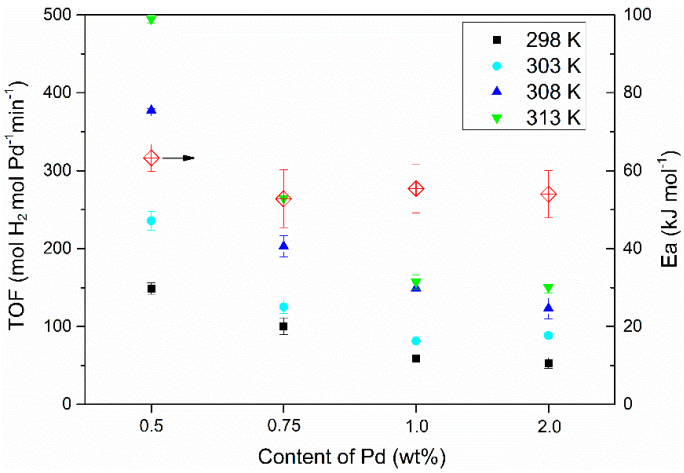

(**c**)

Figure 5. Plots of hydrogen evolution from ammonia borane vs. time over different catalysts at 298 K (**a**), TOFs on Cu@Pd/C-320 (**b**) and PdCu/C (**c**) at different temperatures and the corresponding Ea.

3.3. Effect of Cu(I)

To illustrate the role of Cu(I) during the preparation of catalysts, Cu/C with different Cu_2O content were prepared and used for the synthesis of Cu@Pd/C. The oxidization degree of Cu on Cu/C was controlled by changing the amount of air injected. The XRD patterns of Cu/C are shown in Figure 6a. After the carbothermal reduction in N_2, diffraction peaks corresponding to metallic Cu were observed in Cu/C, and no diffraction peaks of Cu_2O were found in the XRD pattern. Then, the air was injected under N_2 atmosphere at 498 K to partially oxidize the Cu nanoparticles on Cu/C-0. After the injection of 160 mL of air, diffraction peaks ascribed to Cu_2O emerged in the XRD pattern of Cu/C-160. As the amount of air injected increased, the diffraction peaks corresponding to Cu_2O increased, while those corresponding to Cu decreased. Two tiny diffraction peaks (35.5° and 38.7°) ascribed to CuO could be observed on Cu/C-480. When 640 mL of air was injected, diffraction peaks of metallic Cu disappeared, and the peaks of CuO enlarged a little. It is obvious that the Cu was controllably oxidized to Cu_2O by the injected air, and the large amount of air led to the presence of CuO. The oxidation states of the surface Cu were further characterized by XPS (Figure 6b) and AES (Figure 6c). The satellite peak of CuO at 943.4 eV in the XPS spectra was not obvious in all the Cu/C samples except for Cu/C-640. The Cu/C-640 sample showed a tiny but obvious CuO satellite peak in the XPS spectra [81]. This showed that the CuO was not the main species on the surface of Cu nanoparticles. However, the peak areas of CuO at 933.7 eV did increase as the amount of air increased. As the Cu_2O and Cu had similar binding energy in the XPS spectra, the AES spectra was employed to distinguish the Cu_2O and Cu. The binding energy at 568.5 eV was considered to be the signal of CuO and Cu [81,82]. The low content of CuO on the surface was revealed by the XPS results, which showed that this 568.5 eV peak was mostly caused by the metallic Cu. The peak centered at 570.0 eV was ascribed to the Cu_2O [81,82]. It could be seen that there was a small portion of Cu_2O in Cu/C-0 after the carbothermal reduction in N_2. This could be caused by the short exposure to air during the preparation process. As the amount of air injected increased, the peak ascribed to Cu_2O increased, while the peak ascribed to Cu decreased. The results indicated that more and more metallic Cu was oxidized on the surface as more air was introduced. The content of Cu species on the surface could be easily regulated by the control of air injected.

The Cu/C with different Cu_2O content was used for the preparation of Cu@Pd/C by the galvanic reduction method. The hydrolysis of AB was conducted to evaluate the Cu@Pd/C prepared from Cu/C with different Cu_2O content. The results are shown in Figure 7. The TOF on Cu@Pd/C-0 was 180 mol_{H2} min^{-1} $mol_{Pd}{}^{-1}$, which was much higher than the TOF on commercial Pd/C and $Pd_{0.5}Cu/C$ prepared by the impregnation method, showing the superiority of the galvanic reduction method. The activity could be further improved by the partial oxidation of the surface of Cu nanoparticles on Cu/C before the galvanic reduction process. The TOF increased as the surface oxidation of Cu was enhanced. The reason for this increase could be explicated as follows. The surface of Cu nanoparticles was divided by Cu(I) into discrete pieces of metallic Cu, which acted as a reducing agent for Pd(II). The Cu(I) did not react with the Pd(II) during the galvanic reduction process. As a result, the reduced Pd(0) was confined to the original position of Cu(0), and the aggregation of Pd(0) was restricted by the Cu(I) during the preparation process. The best TOF value (465 mol_{H2} min^{-1} $mol_{Pd}{}^{-1}$) was acquired on Cu@Pd/C-640 owing to its highest content of Cu_2O. Table 1 summarizes the TOF values for the reported palladium catalysts in the hydrolysis of AB. It can be seen that the TOF values on Cu@Pd/C were among the highest TOF values reported in the literature.

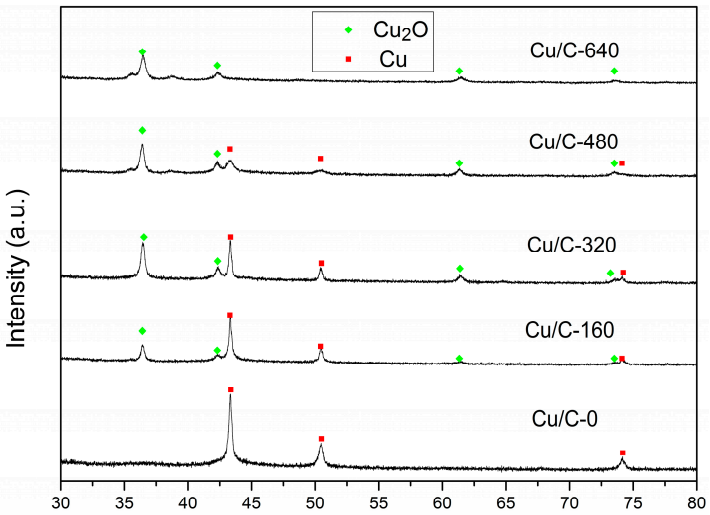

(**a**)

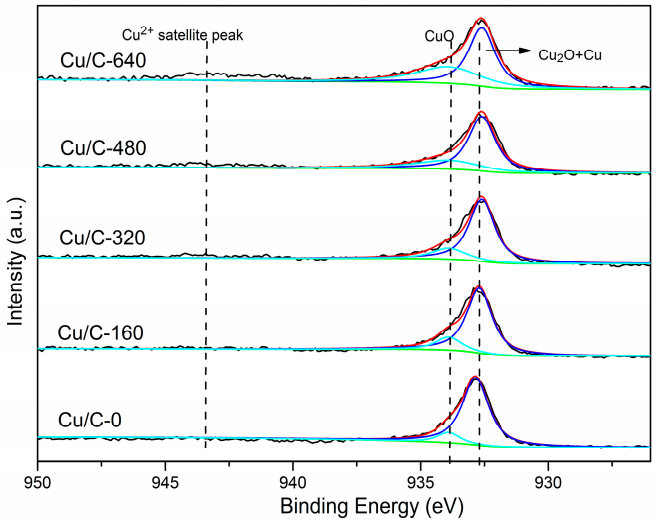

(**b**)

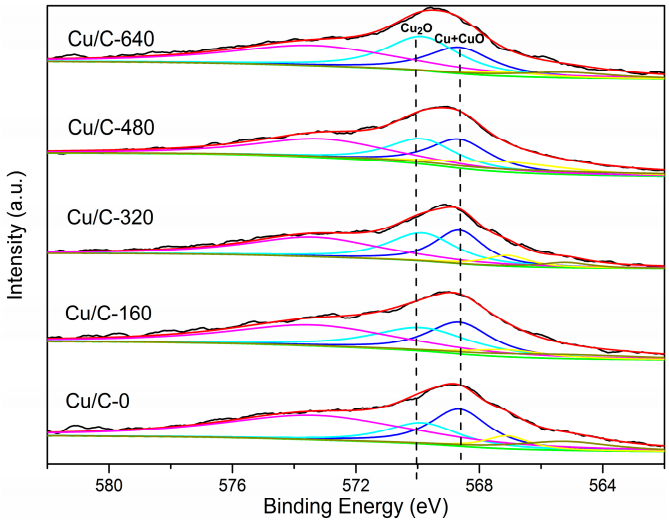

(**c**)

Figure 6. XRD patterns (**a**) XPS (**b**) and auger electron spectroscopy (AES) spectra (**c**) of Cu/C with different oxidation degrees.

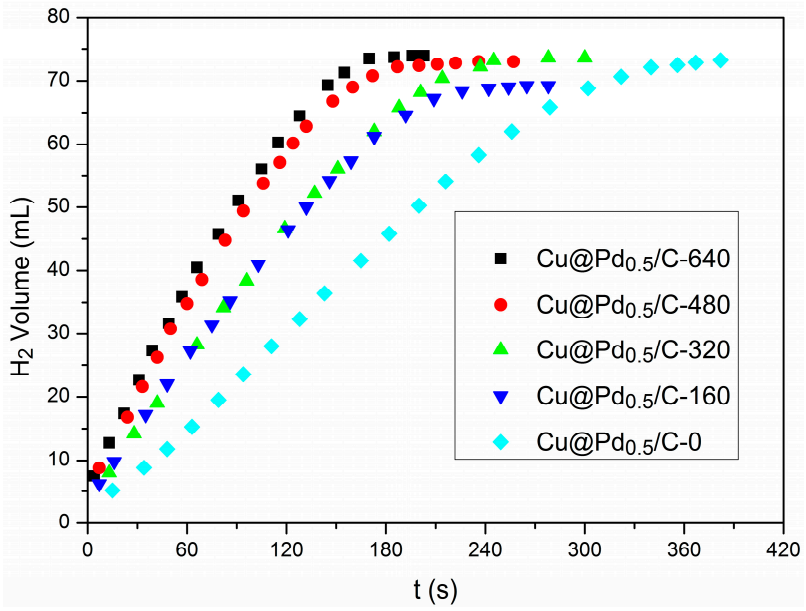

(**a**)

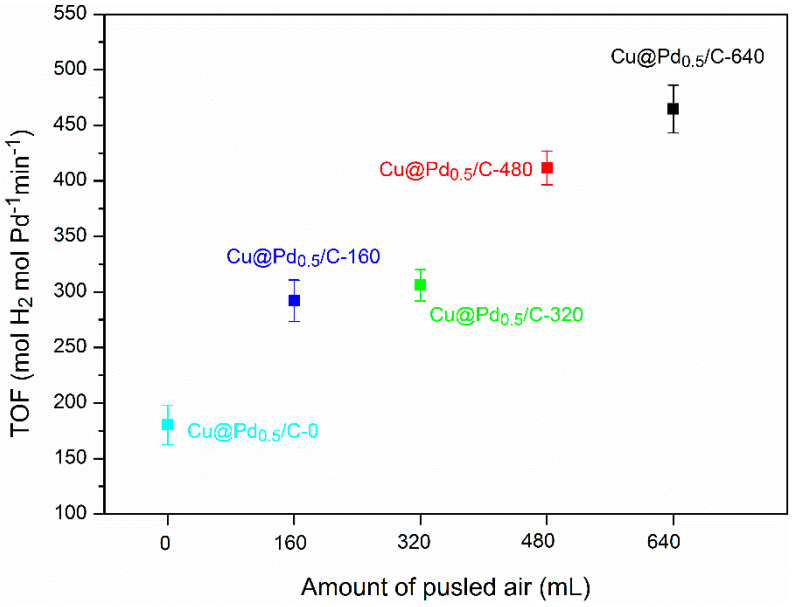

(**b**)

Figure 7. Plots of hydrogen evolution from ammonia borane vs. time over Cu@Pd/C prepared from Cu/C with different oxidation degrees (**a**) and the corresponding turnover frequencies (TOFs) (**b**).

Table 1. Catalytic activity for the reported palladium catalysts in the hydrolysis of ammonia borane (AB).

Entry	Catalysts	Temperature (K)	TOF (mol_{H2} min^{-1} $mol_{Pd}{}^{-1}$)	*Ea* (kJ mol^{-1})	Ref.
1	$Cu@Pd_{0.5}/C$-640	298	465	-	This work
2	$Cu@Pd_{0.5}/C$-320	298	306	57	This work
3	$Pd^0/CoFe_2O_4$	298	290	42	[38]
4	$Pd(0)/SiO_2–CoFe_2O_4$	298	254	52	[33]
5	$Pd_{74}Ni_{26}$/MCN	rt	247	54	[39]
6	Pd@UiO-66	353	231	37	[40]
7	Pd/RCC3	303	176	-	[11]
8	Pd^0/PDA–$CoFe_2O_4$	298	175	65	[38]
9	Pd/IPCNs	298	113	29	[29]
10	Pd/AC	303	40	68	[32]
11	Pd^0/CeFe	298	29	-	[28]
12	$Pd(0)/g\text{-}C_3N_4$-CS	303	28	35	[15]
13	Pd/CGP-GO-Fe_3O_4	303	27	37	[36]
14	Pd(0)/GO-ILCS	303	26	38	[14]
15	$Pd(0)/CS\text{-}Fe_3O_4$	303	15	36	[37]

3.4. Catalyst Stability

The stability of the catalysts was studied using $Cu@Pd_{0.5}/C$-320 as catalysts at 298 K. After each reaction, another 1 mmol of AB was added into the reactor to record the hydrogen released from AB vs. time. The results are shown in Figure 8 and Figure S10. The catalytic performance was well maintained in five continuous processes. The used catalyst $Cu@Pd_{0.5}/C$-320-R was characterized by EDS mapping (Figure S4), HRTEM (Figure S13), TEM (Figure S14), and ICP-OES (Table S1). The content of Pd was well kept after the five recycles indicated by the ICP-OES characterization (Table S1). No agglomerated palladium particles were observed, as there had been no crystalline domains corresponding to Pd in the HRTEM (Figure S13), and the TEM mappings exhibited a uniform distribution of Pd (Figure S4). These results showed very well the reusable performance of the Cu@Pd/C catalysts.

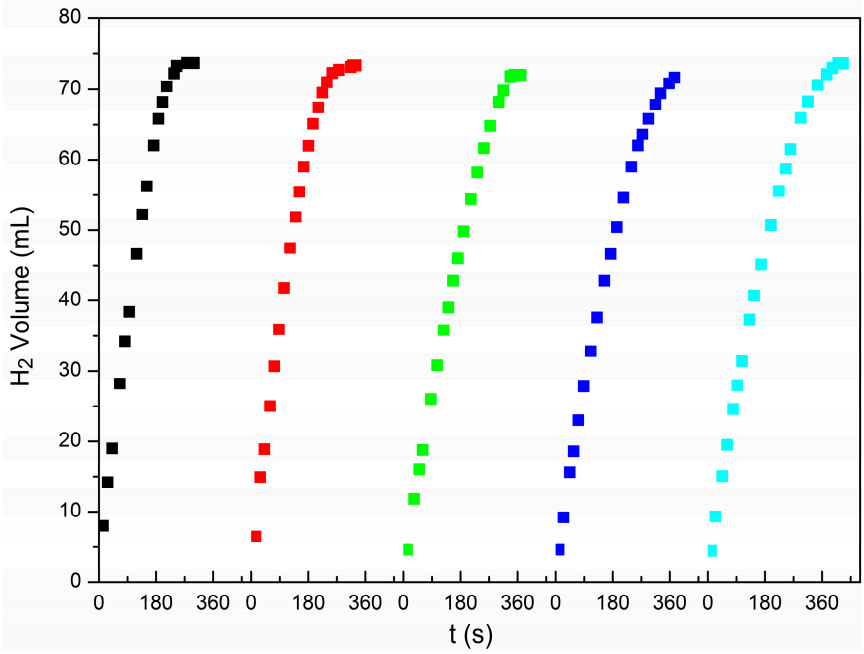

Figure 8. The stability test of $Cu@Pd_{0.5}/C$-320.

4. Conclusions

In summary, the pulse oxidation was an effective method to regulate the oxidation degree of Cu in Cu/C catalysts, which could control the dispersion of Pd on Cu nanoparticles in the preparation of Cu@Pd/C catalysts by the galvanic reduction method. Surface Pd-rich Cu@Pd/C catalysts were allowed to form by the galvanic reduction method and had more superior catalytic performance in the hydrolysis of AB compared to the traditional method. The Cu(I) in the partially oxidized Cu/C did not react with Pd(II) and restricted the reduction location of Pd(II) as well as the aggregation of Pd(0) to form high-performance catalysts for the hydrolysis of AB. The TOF for the hydrolysis of AB reached 465 mol_{H2} min^{-1} $mol_{Pd}{}^{-1}$ on $Cu@Pd_{0.5}$/C-640. The catalysts had good stability in five continuous processes, which makes them promising candidates in the practical application of hydrogen evolution from ammonia borane. The manuscript also provides good inspiration for the preparation of high-performance noble metal-based catalysts.

Supplementary Materials: The following are available online at http://www.mdpi.com/2079-4991/10/9/1850/s1, Figure S1: EDS mapping images of $Cu@Pd_{0.75}$/C-320, Figure S2: EDS mapping images of $Cu@Pd_{1.0}$/C-320, Figure S3: EDS mapping images of $Cu@Pd_{2.0}$/C-320, Figure S4: EDS mapping images of $Cu@Pd_{0.5}$/C-320-R, Figures S5 and S6: Plots of hydrogen evolution from ammonia borane vs. time on Cu@Pd/C-320 at 298 K (a), 303 K (b), 308 K (c), 313 K (d) and the corresponding Arrhenius plot (e), Figures S7 and S8: Plots of hydrogen evolution from ammonia borane vs. time on PdCu/C at 298 K (a), 303 K (b), 308 K (c), 313 K (d), and the corresponding Arrhenius plot (e), Figure S9: Plots of hydrogen evolution from ammonia borane vs. time over Cu@Pd/C prepared from Cu/C with different oxidation degree, Figure S10: The stability test of Cu@Pd0.5/-320, Figure S11: Survey XPS spectra of PdCu/C and Cu@Pd/C, Figure S12: Survey XPS spectra of Cu/C, Figure S13: The HRTEM image of $Cu@Pd_{0.5}$/C-320-R, Figure S14: TEM image of $Cu@Pd_{0.5}$/C-320-R, Figure S15: The schematic diagram of apparatus for catalytic hydrolysis of AB, Table S1: The content of Pd and Cu in the sample determined by ICP-OES.

Author Contributions: Conceptualization, X.G. and Y.Y.; methodology, D.S.; data curation, D.L.; writing—original draft preparation, Y.D.; writing—review and editing, Y.Y.; visualization, D.D.; supervision, X.G.; funding acquisition, Y.Y. and Y.D. All authors have read and agreed to the published version of the manuscript.

Funding: This research was funded by the National Natural Science Foundation of China (21902071 and 21801110) and Intercollegiate Key Scientific Research Projects of Henan Province (19B150012).

Conflicts of Interest: The authors declare no conflict of interest.

References

1. Zhan, W.-W.; Zhu, Q.-L.; Xu, Q. Dehydrogenation of Ammonia Borane by Metal Nanoparticle Catalysts. *ACS Catal.* **2016**, *6*, 6892–6905. [CrossRef]
2. Alpaydın, C.; KarahanGülbay, S.; Colpan, C.O. A Review on the Catalysts Used for Hydrogen Production from Ammonia Borane. *Int. J. Hydrogen Energy* **2020**, *45*, 3414–3434. [CrossRef]
3. Demirci, U.B. Ammonia Borane, a Material with Exceptional Properties for Chemical Hydrogen Storage. *Int. J. Hydrogen Energy* **2017**, *42*, 9978–10013. [CrossRef]
4. Akbayrak, S.; Özkar, S. Ammonia Borane as Hydrogen Storage Materials. *Int. J. Hydrogen Energy* **2018**, *43*, 18592–18606. [CrossRef]
5. Jiang, H.-L.; Xu, Q. Catalytic Hydrolysis of Ammonia Borane for Chemical Hydrogen Storage. *Catal. Today* **2011**, *170*, 56–63. [CrossRef]
6. Lang, C.; Jia, Y.; Yao, X. Recent Advances in Liquid-phase Chemical Hydrogen Storage. *Energy Storage Mater.* **2020**, *26*, 290–312. [CrossRef]
7. Wang, K.; Pan, Z.; Yu, X. Metal B-N-H Hydrogen-Storage Compound: Development and Perspectives. *J. Alloys Compd.* **2019**, *794*, 303–324. [CrossRef]
8. Boom, D.H.A.; Jupp, A.R.; Slootweg, J.C. Dehydrogenation of Amine–Boranes Using p-Block Compounds. *Chem.-Eur. J.* **2019**, *25*, 9133–9152. [CrossRef]
9. Sun, Q.; Wang, N.; Xu, Q.; Yu, J. Nanopore-Supported Metal Nanocatalysts for Efficient Hydrogen Generation from Liquid-Phase Chemical Hydrogen Storage Materials. *Adv. Mater.* **2020**, e2001818. [CrossRef]
10. Sanyal, U.; Demirci, U.B.; Jagirdar, B.R.; Miele, P. Hydrolysis of Ammonia Borane as a Hydrogen Source: Fundamental Issues and Potential Solutions Towards Implementation. *ChemSusChem* **2011**, *4*, 1731–1739. [CrossRef]

11. Yang, X.; Sun, J.-K.; Kitta, M.; Pang, H.; Xu, Q. Encapsulating Highly Catalytically Active Metal Nanoclusters inside Porous Organic Cages. *Nat. Catal.* **2018**, *1*, 214–220. [CrossRef]
12. Sun, Q.; Wang, N.; Zhang, T.; Bai, R.; Mayoral, A.; Zhang, P.; Zhang, Q.; Terasaki, O.; Yu, J. Zeolite-Encaged Single-Atom Rh Catalysts: Highly-Efficient Hydrogen Generation and Shape-Selective Tandem Hydrogenation of Nitroarenes. *Angew. Chem. Int. Ed.* **2019**, *58*, 18570–18576. [CrossRef] [PubMed]
13. Telleria, A.; Vicent, C.; Nacianceno, V.S.; Garralda, M.A.; Freixa, Z. Experimental Evidence Supporting Related Mechanisms for Ru(II)-Catalyzed Dehydrocoupling and Hydrolysis of Amine-Boranes. *ACS Catal.* **2017**, *7*, 8394–8405. [CrossRef]
14. Jia, H.; Chen, X.; Liu, C.-Y.; Liu, X.-J.; Zheng, X.-C.; Guan, X.-X.; Liu, P. Ultrafine Palladium Nanoparticles Anchoring Graphene Oxide-ionic Liquid Grafted Chitosan Self-assembled Materials: The Novel Organic-inorganic Hybrid Catalysts for Hydrogen Generation in Hydrolysis of Ammonia Borane. *Int. J. Hydrogen Energy* **2018**, *43*, 12081–12090. [CrossRef]
15. Jia, H.; Chen, X.; Song, X.; Zheng, X.; Guan, X.; Liu, P. Graphitic Carbon Nitride-chitosan Composites–anchored Palladium Nanoparticles as High-performance Catalyst for Ammonia Borane Hydrolysis. *Int. J. Energy Res.* **2018**, *43*, 535–543. [CrossRef]
16. Chen, W.; Ji, J.; Duan, X.; Qian, G.; Li, P.; Zhou, X.; Chen, D.; Yuan, W. Unique Reactivity in Pt/CNT Catalyzed Hydrolytic Dehydrogenation of Ammonia Borane. *Chem. Commun.* **2014**, *50*, 2142–2144. [CrossRef]
17. Akbayrak, S.; Tonbul, Y.; Özkar, S. Ceria Supported Rhodium Nanoparticles: Superb Catalytic Activity in Hydrogen Generation from the Hydrolysis of Ammonia Borane. *Appl. Catal. B Environ.* **2016**, *198*, 162–170. [CrossRef]
18. Chen, J.; Hu, M.; Ming, M.; Xu, C.; Wang, Y.; Zhang, Y.; Wu, J.; Gao, D.; Bi, J.; Fan, G. Carbon-supported Small Rh Nanoparticles Prepared with Sodium Citrate: Toward High Catalytic Activity for Hydrogen Evolution from Ammonia Borane Hydrolysis. *Int. J. Hydrogen Energy* **2018**, *43*, 2718–2725. [CrossRef]
19. Akbayrak, S.; Tonbula, Y.; Özkar, S. Ceria-Supported Ruthenium Nanoparticles as Highly Active and Long-Lived Catalyst in Hydrogen Generation from the Hydrolysis of Ammonia Borane. *Dalton Trans.* **2016**, *27*, 10969–10978. [CrossRef]
20. Wang, H.; Xu, C.; Chen, Q.; Ming, M.; Wang, Y.; Sun, T.; Zhang, Y.; Gao, D.; Bi, J.; Fan, G. Nitrogen-Doped Carbon Stabilized Ru Nanoclusters as Excellent Catalyst for Hydrogen Production. *ACS Sustain. Chem. Eng.* **2018**, *7*, 1178–1184. [CrossRef]
21. Axet, M.R.; Philippot, K. Catalysis with Colloidal Ruthenium Nanoparticles. *Chem. Rev.* **2020**, *120*, 1085–1145. [CrossRef] [PubMed]
22. Han, C.; Meng, P.; Waclawik, E.R.; Zhang, C.; Li, X.-H.; Yang, H.; Antonietti, M.; Xu, J. Pd/g-C3N4 Stabilized Emulsion Microreactor as a Temporal Hydrogen Storage for Full Use of Hydrogen from Ammonia Borane toward Efficient Alkene Hydrogenation. *Angew. Chem. Int. Ed.* **2018**, *57*, 14857–14861. [CrossRef] [PubMed]
23. Zhang, X.; Kam, L.; Trerise, R.; Williams, T.J. Ruthenium-Catalyzed Ammonia Borane Dehydrogenation: Mechanism and Utility. *Acc. Chem. Res.* **2017**, *50*, 86–95. [CrossRef]
24. Fang, Y.; Li, J.; Togo, T.; Jin, F.; Xiao, Z.; Liu, L.; Drake, H.; Lian, X.; Zhou, H.-C. Ultra-Small Face-Centered-Cubic Ru Nanoparticles Confined within a Porous Coordination Cage for Dehydrogenation. *Chem* **2018**, *4*, 555–563. [CrossRef]
25. Rej, S.; Hsia, C.-F.; Chen, T.-Y.; Lin, F.-C.; Huang, J.-S.; Huang, M.H. Facet-Dependent and Light-Assisted Efficient Hydrogen Evolution from Ammonia Borane Using Gold-Palladium Core-Shell Nanocatalysts. *Angew. Chem. Int. Ed.* **2016**, *55*, 7222–7226. [CrossRef]
26. Hu, M.; Ming, M.; Xu, C.; Wang, Y.; Zhang, Y.; Gao, D.; Bi, J.; Fan, G. Towards High-Efficiency Hydrogen Production through in situ Formation of Well-Dispersed Rhodium Nanoclusters. *ChemSusChem* **2018**, *11*, 3253–3258. [CrossRef]
27. Chen, W.; Duan, X.; Qian, G.; Chen, D.; Zhou, X. Carbon Nanotubes as Support in the Platinum-Catalyzed Hydrolytic Dehydrogenation of Ammonia Borane. *ChemSusChem* **2015**, *8*, 2927–2931. [CrossRef]
28. Akbayrak, S.; Çakmak, G.; Öztürk, T.; Özkar, S. Rhodium(0), Ruthenium(0) and Palladium(0) Nanoparticles Supported on Carbon-coated Iron: Magnetically Isolable and Reusable Catalysts for Hydrolytic Dehydrogenation of Ammonia Borane. *Int. J. Hydrogen Energy* **2020**. [CrossRef]
29. Mao, M.; Chen, Q.; Wu, J.; Fan, G. Anchoring and Space-confinement Effects to Synthesize Ultrasmall Pd Nanoparticles for Efficient Ammonia Borane Hydrolysis. *Int. J. Hydrogen Energy* **2020**. [CrossRef]

30. Güngörmez, K.; Metin, Ö. Composition-controlled Catalysis of Reduced Graphene Oxide Supported CuPd Alloy Nanoparticles in the Hydrolytic Dehydrogenation of Ammonia Borane. *Appl. Catal. A Gen.* **2015**, *494*, 22–28. [CrossRef]
31. Kılıç, B.; Şencanlı, S.; Metin, Ö. Hydrolytic Dehydrogenation of Ammonia Borane Catalyzed by Reduced Graphene Oxide Supported Monodisperse Palladium Nanoparticles: High Activity and Detailed Reaction Kinetics. *J. Mol. Catal. A* **2012**, *361–362*, 104–110. [CrossRef]
32. Akbayrak, S.; Ozcifci, Z.; Tabak, A. Noble Metal Nanoparticles Supported on Activated Carbon: Highly Recyclable Catalysts in Hydrogen Generation from the Hydrolysis of Ammonia Borane. *J. Colloid. Interface Sci.* **2019**, *546*, 324–332. [CrossRef] [PubMed]
33. Akbayrak, S.; Kaya, M.; Volkan, M.; Özkar, S. Palladium(0) Nanoparticles Supported on Silica-coated Cobalt Ferrite: A Highly Active, Magnetically Isolable and Reusable Catalyst for Hydrolytic Dehydrogenation of Ammonia Borane. *Appl. Catal. B Environ.* **2014**, *147*, 387–393. [CrossRef]
34. Xi, P.; Chen, F.; Xie, G.; Ma, C.; Liu, H.; Shao, C.; Wang, J.; Xu, Z.; Xu, X.; Zeng, Z. Surfactant Free RGO/Pd Nanocomposites as Highly Active Heterogeneous Catalysts for the Hydrolytic Dehydrogenation of Ammonia Borane for Chemical Hydrogen Storage. *Nanoscale* **2012**, *4*, 5597–5601. [CrossRef]
35. Wang, J.; Qin, Y.-L.; Liu, X.; Zhang, X.-B. In Situ Synthesis of Magnetically Recyclable Graphene-supported Pd@Co Core–shell Nanoparticles as Efficient Catalysts for Hydrolytic Dehydrogenation of Ammonia Borane. *J. Mater. Chem.* **2012**, *22*, 12468–12470. [CrossRef]
36. Jia, H.; Liu, S.; Zheng, G.-P.; Zheng, X.-C.; Wang, X.-Y.; Liu, P. Collagen-graphene Oxide Magnetic Hybrids Anchoring Pd(0) Catalysts for Efficient H_2 Generation from Ammonia Borane. *Int. J. Hydrogen Energy* **2019**, *44*, 27022–27029. [CrossRef]
37. Jia, H.; Liu, X.-J.; Chen, X.; Guan, X.-X.; Zheng, X.-C.; Liu, P. Chitosan-Fe_3O_4 Anchored Palladium Nanoparticles: An Efficiently Magnetic Catalyst for Hydrolytic Dehydrogenation of Ammonia Borane. *Int. J. Hydrogen Energy* **2017**, *42*, 28425–28433. [CrossRef]
38. Manna, J.; Akbayrak, S.; Özkar, S. Palladium(0) nanoparticles supported on polydopamine coated $CoFe_2O_4$ as highly active, magnetically isolable and reusable catalyst for hydrogen generation from the hydrolysis of ammonia borane. *Appl. Catal. B Environ.* **2017**, *208*, 104–115. [CrossRef]
39. Wang, W.; Lu, Z.-H.; Luo, Y.; Zou, A.; Yao, Q.; Chen, X. Mesoporous Carbon Nitride Supported Pd and Pd-Ni Nanoparticles as Highly Efficient Catalyst for Catalytic Hydrolysis of NH_3BH_3. *ChemCatChem* **2018**, *10*, 1620–1626. [CrossRef]
40. Bakuru, V.R.; Velaga, B.; Peela, N.R.; Kalidindi, S.B. Hybridization of Pd Nanoparticles with UiO-66(Hf) Metal-Organic Framework and the Effect of Nanostructure on the Catalytic Properties. *Chem.-Eur. J.* **2018**, *24*, 15978–15982. [CrossRef] [PubMed]
41. Filiz, B.C.; Figen, A.K.; Pişkin, S. The Remarkable Role of Metal Promoters on the Catalytic Activity of Co-Cu Based Nanoparticles for Boosting Hydrogen Evolution: Ammonia Borane Hydrolysis. *Appl. Catal. B Environ.* **2018**, *238*, 365–380. [CrossRef]
42. Liu, Y.; Zhang, J.; Guan, H.; Zhao, Y.; Yang, J.-H.; Zhang, B. Preparation of Bimetallic Cu-Co Nanocatalysts on Poly (diallyldimethylammonium chloride) Functionalized Halloysite Nanotubes for Hydrolytic Dehydrogenation of Ammonia Borane. *Appl. Surf. Sci.* **2018**, *427*, 106–113. [CrossRef]
43. Zhang, J.; Li, H.; Zhang, H.; Zhu, Y.; Mi, G. Porously Hierarchical Cu@Ni Cubic-cage Microstructure: Very Active and Durable Catalyst for Hydrolytically Liberating H_2 Gas from Ammonia Borane. *Renew. Energy* **2016**, *99*, 1038–1045. [CrossRef]
44. Li, J.; Zhu, Q.-L.; Xu, Q. Non-noble Bimetallic CuCo Nanoparticles Encapsulated in the Pores of Metal–organic Frameworks: Synergetic Catalysis in the Hydrolysis of Ammonia Borane for Hydrogen Generation. *Catal. Sci. Technol.* **2015**, *5*, 525–530. [CrossRef]
45. Wang, C.; Wang, H.; Wang, Z.; Li, X.; Chi, Y.; Wang, M.; Gao, D.; Zhao, Z. Mo Remarkably Enhances Catalytic Activity of Cu@MoCo Core-shell Nanoparticles for Hydrolytic Dehydrogenation of Ammonia Borane. *Int. J. Hydrogen Energy* **2018**, *43*, 7347–7355. [CrossRef]
46. Qu, X.; Jiang, R.; Li, Q.; Zeng, F.; Zheng, X.; Xu, Z.; Chen, C.; Peng, J. The Hydrolysis of Ammonia Borane Catalyzed by NiCoP/OPC-300 Nanocatalysts: High Selectivity and Efficiency, and Mechanism. *Green Chem.* **2019**, *21*, 850–860. [CrossRef]

47. Li, P.Z.; Aijaz, A.; Xu, Q. Highly Dispersed Surfactant-free Nickel Nanoparticles and Their Remarkable Catalytic Activity in the Hydrolysis of Ammonia Borane for Hydrogen Generation. *Angew. Chem. Int. Ed.* **2012**, *51*, 6753–6756. [CrossRef]
48. Yao, Q.; Lu, Z.-H.; Yang, Y.; Chen, Y.; Chen, X.; Jiang, H.-L. Facile Synthesis of Graphene-supported Ni-CeOx Nanocomposites as Highly Efficient Catalysts for Hydrolytic Dehydrogenation of Ammonia Borane. *Nano Res.* **2018**, *11*, 4412–4422. [CrossRef]
49. Feng, K.; Zhong, J.; Zhao, B.; Zhang, H.; Xu, L.; Sun, X.; Lee, S.-T. $Cu_xCo_{1-x}O$ Nanoparticles on Graphene Oxide as A Synergistic Catalyst for High-Efficiency Hydrolysis of Ammonia–Borane. *Angew. Chem. Int. Ed.* **2016**, *55*, 11950–11954. [CrossRef]
50. Liu, P.; Gu, X.; Kang, K.; Zhang, H.; Cheng, J.; Su, H. Highly Efficient Catalytic Hydrogen Evolution from Ammonia Borane Using the Synergistic Effect of Crystallinity and Size of Noble-MetalFree Nanoparticles Supported by Porous Metal-Organic Frameworks. *ACS Appl. Mater. Interfaces* **2017**, *9*, 10759–10767. [CrossRef]
51. Du, J.; Hou, J.; Li, B.; Qin, R.; Xu, C.; Liu, H. Support-free 3D Hierarchical Nanoporous $Cu@Cu_2O$ for Fast Tandemm Ammonia Borane Dehydrogenation and Nitroarenes Hydrogenation under Mild Conditions. *J. Alloys Compd.* **2020**, *815*, 152372. [CrossRef]
52. Wang, C.; Tuninetti, J.; Wang, Z.; Zhang, C.; Ciganda, R.; Salmon, L.; Moya, S.; Ruiz, J.; Astruc, D. Hydrolysis of Ammonia-Borane over Ni/ZIF-8 Nanocatalyst: High Efficiency, Mechanism, and Controlled Hydrogen Release. *J. Am. Chem. Soc.* **2017**, *139*, 11610–11615. [CrossRef] [PubMed]
53. Wang, Y.; Shen, G.; Zhang, Y.; Pan, L.; Zhang, X.; Zou, J.-J. Visible-light-induced Unbalanced Charge on $NiCoP/TiO_2$ Sensitized System for Rapid H_2 Generation from Hydrolysis of Ammonia Borane. *Appl. Catal. B Environ.* **2020**, *260*, 118183. [CrossRef]
54. Ding, R.; Chen, Q.; Luo, Q.; Zhou, L.; Wang, Y.; Zhang, Y.; Fan, G. Salt Template-assisted in situ Construction of Ru Nanoclusters and Porous Carbon: Excellent Catalysts toward Hydrogen Evolution, Ammonia-borane Hydrolysis, and 4-nitrophenol Reduction. *Green Chem.* **2020**, *22*, 835–842. [CrossRef]
55. Chen, M.-J.; Zhang, D.-X.; Li, D.; Ke, S.-C.; Ma, X.-C.; Chang, G.-G.; Chena, J.; Yang, X.-Y. All-around Coating of CoNi Nanoalloy by Hierarchically Porous Carbon Derived from Bimetallic MOFs for Highly Efficient Hydrolytic Dehydrogenation of Ammonia-borane. *New J. Chem.* **2020**, *44*, 3021–3027. [CrossRef]
56. Zhang, L.; Zhou, L.; Yang, K.; Gao, D.; Huang, C.; Chen, Y.; Zhang, F.; Xiong, X.; Li, L.; Xia, Q. Pd Ni Nanoparticles Supported on MIL-101 as High-performance Catalysts for Hydrogen Generation from Ammonia Borane. *J. Alloys Compd.* **2016**, *677*, 87–95. [CrossRef]
57. Cui, X.; Li, H.; Yu, G.; Yuan, M.; Yang, J.; Xu, D.; Hou, Y.; Dong, Z. Pt Coated Co Nanoparticles Supported on N-doped Mesoporous Carbon as Highly Efficient, Magnetically Recyclable and Reusable Catalyst for Hydrogen Generation from Ammonia Borane. *Int. J. Hydrogen Energy* **2017**, *42*, 27055–27065. [CrossRef]
58. Yang, J.; Cui, Z.; Ma, J.; Dong, Z. Ru Coated Co Nanoparticles Decorated on Cotton Derived Carbon Fibers as a Highly Efficient and Magnetically Recyclable Catalyst for Hydrogen Generation from Ammonia Borane. *Int. J. Hydrogen Energy* **2018**, *43*, 1355–1364. [CrossRef]
59. Shang, N.; Zhou, X.; Feng, C.; Gao, S.; Wu, Q.; Wang, C. Synergetic Catalysis of Ni Pd Nanoparticles Supported on Biomass-derived Carbon Spheres for Hydrogen Production from Ammonia Borane at Room Temperature. *Int. J. Hydrogen Energy* **2017**, *42*, 5733–5740. [CrossRef]
60. Zhang, J.; Chen, W.; Ge, H.; Chen, C.; Yan, W.; Gao, Z.; Gan, J.; Zhang, B.; Duan, X.; Qin, Y. Synergistic Effects in Atomic-layer-deposited PtCox/CNTs Catalysts Enhancing Hydrolytic Dehydrogenation of Ammonia Borane. *Appl. Catal. B Environ.* **2018**, *235*, 256–263. [CrossRef]
61. Xiong, X.; Zhou, L.; Yu, G.; Yang, K.; Ye, M.; Xia, Q. Synthesis and Catalytic Performance of a Novel RuCuNi/CNTs Nanocomposite in Hydrolytic Dehydrogenation of Ammonia Borane. *Int. J. Hydrogen Energy* **2015**, *40*, 15521–15528. [CrossRef]
62. Li, Z.; He, T.; Matsumura, D.; Miao, S.; Wu, A.; Liu, L.; Wu, G.; Chen, P. Atomically Dispersed Pt on the Surface of Ni Particles: Synthesis and Catalytic Function in Hydrogen Generation from Aqueous Ammonia–borane. *ACS Catal.* **2017**, *7*, 6762–6769. [CrossRef]
63. Fu, F.; Wang, C.; Wang, Q.; Martinez-Villacorta, A.M.; Escobar, A.; Chong, H.; Wang, X.; Moya, S.; Salmon, L.; Fouquet, E.; et al. Highly Selective and Sharp Volcano-type Synergistic $Ni_2Pt@ZIF$-8-Catalyzed Hydrogen Evolution from Ammonia Borane Hydrolysis. *J. Am. Chem. Soc.* **2018**, *140*, 10034–10042. [CrossRef] [PubMed]

64. Wang, Q.; Fu, F.; Yang, S.; Moro, M.M.; Ramirez, M.d.l.A.; Moya, S.; Salmon, L.; Ruiz, J.; Astruc, D. Dramatic Synergy in CoPt Nanocatalysts Stabilized by "Click"Dendrimers for Evolution of Hydrogen from Hydrolysis of Ammonia Borane. *ACS Catal.* **2019**, *9*, 1110–1119. [CrossRef]
65. Zhu, M.-M.; Du, X.-L.; Zhao, Y.; Mei, B.-B.; Zhang, Q.; Sun, F.-F.; Jiang, Z.; Liu, Y.-M.; He, H.-Y.; Cao, Y. Ring-Opening Transformation of 5-Hydroxymethylfurfural Using a Golden Single-Atomic-Site Palladium Catalyst. *ACS Catal.* **2019**, *9*, 6212–6222. [CrossRef]
66. You, L.; Mao, Y.; Ge, J. Synthesis of Stable SiO_2@Au-Nanoring Colloids as Recyclable Catalysts: Galvanic Replacement Taking Place on the Surface. *J. Phys. Chem. C* **2012**, *116*, 10753–10759. [CrossRef]
67. Mahara, Y.; Ohyama, J.; Sawabe, K.; Satsuma, A. Synthesis of Supported Bimetal Catalysts using Galvanic Deposition Method. *Chem. Rec.* **2018**, *18*, 1306–1313. [CrossRef]
68. Mintsouli, I.; Georgieva, J.; Armyanov, S.; Valova, E.; Avdeev, G.; Hubin, A.; Steenhaut, O.; Dille, J.; Tsiplakides, D.; Balomenou, S.; et al. Pt-Cu Electrocatalysts for Methanol Oxidation Prepared by Partial Galvanic Replacement of Cu/carbon Powder Precursors. *Appl. Catal. B Environ.* **2013**, *136–137*, 160–167. [CrossRef]
69. Zhou, G.; Wang, H.; Tian, J.; Pei, Y.; Fan, K.; Qiao, M.; Sun, B.; Zong, B. Ru-Zn/ZrO2 Nanocomposite Catalysts Fabricated by Galvanic Replacement for Benzene Partial Hydrogenation. *ChemCatChem* **2018**, *10*, 1184–1191. [CrossRef]
70. Zhang, Y.; Diao, W.; Monnier, J.R.; Williams, C.T. Pd-AgSiO_2 Bimetallic Catalysts Prepared by Galvanic Displacement for Selective Hydrogenation of Acetylene in Excesse Thylene. *Catal. Sci. Technol.* **2015**, *5*, 4123–4132. [CrossRef]
71. Kobayashi, Y.; Cai, Z.; Chang, G.; He, Y.; Oyama, M. Palladium Deposition on Nickel Microparticles by a Galvanic Replacement Reaction for Electrocatalytic Oxidation of Ethanol. *ACS Appl. Energy Mater.* **2019**, *2*, 6023–6030. [CrossRef]
72. Rodrigues, T.S.; da Silva, A.G.M.; Camargo, P.H.C. Nanocatalysis by Noble Metal Nanoparticles: Controlled Synthesis for the Optimization and Understanding of Activities. *J. Mater. Chem. A* **2019**, *7*, 5857–5874. [CrossRef]
73. Duan, Y.; Zheng, M.; Li, D.; Deng, D.; Wu, C.; Yang, Y. Synthesis of Pd/SBA-15 Catalyst Employing Surface-bonded Vinyl as a Reductant and its Application in the Hydrogenation of Nitroarenes. *RSC Adv.* **2017**, *7*, 3443–3449. [CrossRef]
74. Duan, Y.; Zheng, M.; Li, D.; Deng, D.; Ma, L.-F.; Yang, Y. Conversion of HMF to Methyl Cyclopentenolone by the Pd/Nb_2O_5 and Ca-Al Catalysts via Two-steps Procedure. *Green Chem.* **2017**, *19*, 5103–5113. [CrossRef]
75. Yang, Y.; Xie, Y.; Zhang, J.; Li, D.; Deng, D.; Duan, Y. Fabrication of Pd/SiO_2 with Controllable Wettability for Enhanced Catalytic Hydrogenation Activity at Ambient H_2 Pressure. *ChemCatChem* **2019**, *11*, 5430–5434. [CrossRef]
76. Yang, Y.; Deng, D.; Sui, D.; Xie, Y.; Li, D.; Duan, Y. Facile Preparation of Pd/UiO-66-v for the Conversion of Furfuryl Alcohol to Tetrahydrofurfuryl Alcohol under Mild Conditions in Water. *Nanomaterials* **2019**, *9*, 1698. [CrossRef]
77. Yu, K.; Ning, G.; Yang, J.; Wang, Y.; Zhang, X.; Qin, Y.; Luan, C.; Yu, L.; Jiang, Y.; Luan, X.; et al. Restructured PtNi on Ultrathin Nickel Hydroxide for Enhanced Performance in Hydrogen Evolution and Methanol Oxidation. *J. Catal.* **2019**, *375*, 267–278. [CrossRef]
78. Yang, Y.; Xie, Y.; Deng, D.; Li, D.; Zheng, M.; Duan, Y. Highly Selective Conversion of HMF to 1-hydroxy-2,5-hexanedione on Pd/MIL-101(Cr). *ChemistrySelect* **2019**, *4*, 11165–11171. [CrossRef]
79. Brun, M.; Berthet, A.; Bertolini, J.C. XPS, AES and Auger Parameter of Pd and PdO. *J. Electron. Spectrosc. Relat. Phenom.* **1999**, *104*, 55–60. [CrossRef]
80. Yang, Y.; Yang, D.; Zhang, C.; Zheng, M.; Duan, Y. Preparation of 1-hydroxy-2,5-hexanedione from HMF by the Combination of Commercial Pd/C and Acetic Acid. *Molecules* **2020**, *25*, 2475. [CrossRef]

81. Platzman, I.; Brener, R.; Haick, H.; Tannenbaum, R. Oxidation of Polycrystalline Copper Thin Films at Ambient Conditions. *J. Phys. Chem. C* **2008**, *112*, 1101–1108. [CrossRef]
82. Wang, Q.-N.; Shi, L.; Li, W.; Li, W.-C.; Si, R.; Schüthc, F.; Lu, A.-H. Cu Supported on Thin Carbon Layer Coated Porous SiO_2 for Efficient Ethanol Dehydrogenation. *Catal. Sci. Technol.* **2018**, *8*, 472–479. [CrossRef]